Resilience of LEO Constellations to Accidental and Intentional Fragmentation Events

Mark A. Sturza, Mark D. Dankberg, and William N. Blount
Viasat, Inc.

ABSTRACT

There is a common belief that "resilience" of a proliferated LEO constellation increases monotonically as the number of satellites in such large (or mega) constellations increases. This paper examines a number of scenarios using a combination of analytical and Monte Carlo tools to evaluate short term effects of accidental or intentional random fragmentation events that may occur in one portion of a constellation on the remaining portions of the constellation. The results show that increasing the number of satellites may significantly increase the number of consequential collision events due to a fragmentation event. As a result, large LEO constellations may impose a significant cost to all constellations due to the associated SST, SSA, and STM activities and also may induce significant consequential collision risk to other nearby constellations. Characterizing this cost in terms of expected debris growth is important for understanding future SST, SSA, and STM requirements, and for designing more resilient constellations. We recommend further study along such tools to evaluate the impact on mission performance resilience of highly proliferated constellations, and also the collision risk and resilience consequence of intentionally targeted kinetic fragmentation events.

1. INTRODUCTION

Low Earth orbit (LEO) space remains a precarious domain to operate in irrespective of the steps taken to mitigate against risks. Even with best-in-class Space Surveillance and Tracking (SST), Space Situational Awareness (SSA), and Space Traffic Management (STM), collisions will inevitably occur as large constellations continue to deploy. The fragments created by each collision increase the debris flux, increasing the likelihood of future collisions. When the debris creation rate exceeds the debris removal rate, due to atmospheric drag or active debris removal means, positive feedback (cascading collisions) occurs, leading to exponential growth in the debris flux and eventually resulting in a flux density that renders some orbits effectively unusable. This paper develops a model that helps examine the extent to which a particular design may increase a LEO constellation's resilience, or increase its fragility, in the face of different types of intentional fragmentation events or other interventions, even if those interventions or attacks only affect neighboring constellations.

Proliferated LEO constellations consisting of thousands of satellites are intended to provide continued coverage even if an appreciable fraction of satellites is no longer functional. The underlying belief is that having more satellites creates more resilience. However, redundancy comes with an often-unconsidered cost—the increased vulnerability of large constellations to fragmentation events. That effect can reduce resilience of a constellation, as well as all nearby constellations such that deploying more satellites results in greater fragility. The purpose of this paper is to introduce models that can quantify resilience and fragility. Fragmentation events can occur either through accident (explosions, collisions) or through intentional attacks (kinetic, directed energy, cyber), latent design or production defects (affecting reliability or maneuverability) or even as a consequence of natural phenomena (solar or other radiation excursions). Fragmentation from such interventions can be instantaneous and certain or can be determined as a predictable random value as a function of time from the triggering event. The probability that at least one satellite in a constellation will be fragmented by an accidental collision increases with the size of the constellation. The 15 November 2021 Russian ASAT test shows that hostile activities by sovereign actors in space represent a very real threat to space safety [1].

While debris are spread above and below the collision altitude by fragmentation, the most significant increase in probability of a subsequent collision occurs for other satellites with similar altitude and inclination as those of the fragmented object (Section 2.1). By design, large LEO constellations concentrate satellites into a few, often only one, altitude/inclination pair (Section 4). This rigid constellation structure makes them less resilient to cascading collisions than the same number of satellites in random orbits. Constellation designs with satellites partitioned among multiple altitude/inclination pairs may also increase the fragility of the overall constellation to fragmentation events initially affecting a subset of its satellites.

Previous work has focused on using "source-sink" models, systems of non-linear differential equations, to model the carrying capacity (i.e., the sustainable satellite population distribution in LEO) of various combinations of orbits and satellite characteristics (such as mass and cross-sectional area) [2] [3]. These models have provided an approach to better estimate future debris propagation using a residual carrying capacity metric that enables comparing holistic global contributions to debris propagation as a function of specific system characteristics and deducing the incremental impact of individual systems and characteristics on LEO carrying capacity. While useful, these models address population dynamics, not the dynamics of individual objects required to assess resilience or fragility to specific fragmentation events.

In this paper, a Monte Carlo (MC) simulation is used to explore the sensitivity (i.e., resilience or fragility) of various constellation architectures to intentional fragmentation events or other interventions. All objects, including debris, are propagated discreetly. The propagator uses analytic methods based on a general perturbation theory to model gravity (through J2) and atmospheric drag (Jacchia 1977 atmospheric model with Blitzer decay model). Fragmentation events are modeled using the EVOLVE 4.0 NASA Standard Breakup Model (SBM) suitably modified to conserve mass. Sufficient Monte Carlo trials are generated to provide high confidence in the results.

A baseline is established by using the simulation to evolve reference large LEO constellations over a 3-year timeframe with the current debris flux background. Once the baseline has been established, the effect of intentional fragmentation events is determined on each constellation.

More specifically, the simulation is used to model the sensitivity of current and proposed large LEO constellations with respect to intentional interventions in which individual satellites are fragmented, such as by an ASAT, and in various combinations. Also, the simulation models events in which all of the satellites in a specific constellation are rendered non-maneuverable simultaneously, such as from the result of a cyber-attack. Non-maneuverable satellites cannot avoid collisions, and thus pose a significantly higher risk of being fragmented by an accidental collision.

The simulation results provide guidelines for designing LEO constellations targeted to applications where resiliency is paramount, including commercial, civil, defense, and security applications. They also inform governmental policy makers and regulators with respect to these matters.

The models used in the simulation are described in Section 2. Section 3 describes the simulation flow. The simulation parameters are provided in Section 4. Section 5 presents the simulation results and Section 6 the conclusions.

2. MODELS

Sections 2.1, 2.2, and 2.3 describe the fragmentation, decay, and gravity models, respectively. The encounter rate model is described in Section 2.4.

2.1 Fragmentation Model

The EVOLVE 4.0 NASA Standard Breakup Model (SBM) for spacecraft [4], as clarified by [5] including mass conservation, is used. The number of fragments from 1 mm to 1 m is determined from a power law distribution characterized by the ejection mass of the fragmenting collision. Several large fragments are added near 1 m, as necessary, to conserve mass.

The SBM fragments are petitioned between 1) lethal trackable (LT) fragments with characteristic lengths from 10 cm to 1 m, and 2) lethal non-trackable (LNT) fragments with characteristic lengths from 1 cm to 10 cm. The transition point between the ranges is a representative value [6]. The trackability of a fragment depends on multiple factors, including orbit altitude and reflection coefficient. The lethality of a fragment also depends on multiple factors, including the momentum of the fragment and the mass of the object with which it is colliding.

The power law relationship for the number of fragments with characteristic length in the interval L_{MIN} (m) to L_{Max} (m) resulting from a fragmenting collision with ejection mass $m_e\ (kg)$ is:

$$N = 0.1{m_e}^{0.75}(L_{MIN}^{-1.71} - L_{MAX}^{-1.71})$$

Where, for a fragmenting collision involving two objects, m_e is the sum of the masses of the objects.

Fig. 1 shows the number of fragments as a function of satellite mass for intra-system collisions of equal mass satellites. Separate curves show the numbers of LT and LNT fragments.

For fragmenting collisions, the cdf for characteristic length is:

$$cdf_{L_C} = 1 - \frac{L_C^{-1.71} - L_{MAX}^{-1.71}}{L_{MIN}^{-1.71} - L_{MAX}^{-1.71}}$$

Which has inverse:

$$L_C = (L_{MAX}^{-1.71} + (L_{MIN}^{-1.71} - L_{MAX}^{-1.71})(1-p))^{-0.585}$$

This inverse cdf is used to transform from a uniform distribution on [0, 1) to the characteristic length distribution.

Fig. 2 shows the fragment diameter distributions for the LT and LNT fragments. These distributions do not include the additional fragments for mass conservation.

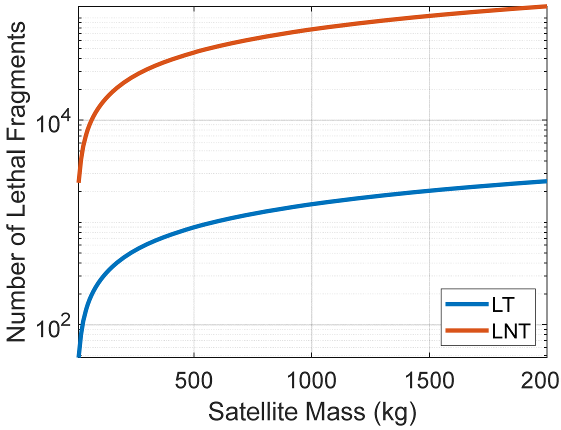

Fig. 1. Number of LT & LNT Fragments v. Satellite Mass

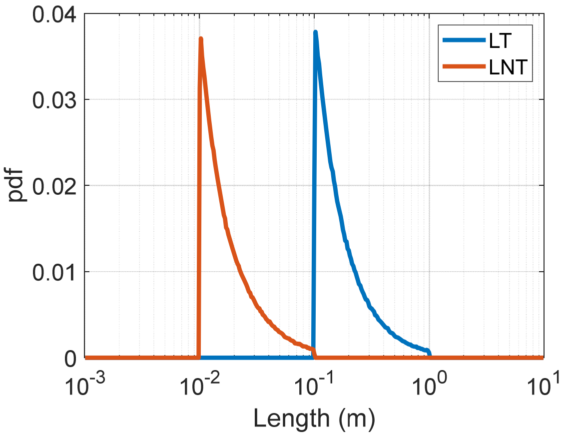

Fig. 2. Characteristic Length Distribution

The SBM characterizes the area-to-mass ratio probability distribution using a normal mixture distribution for $\chi = log_{10}(A/M_F)$ parametrized on $\delta = log_{10}(L_F)$:

$$pdf_\chi = \alpha\mathcal{N}(\chi;\mu_1,\sigma_1) + (1-\alpha)\mathcal{N}(\chi;\mu_1,\sigma_1)$$

where

$$\mathcal{N}(z;\mu,\sigma) = \frac{1}{\sigma\sqrt{2\pi}}e^{-\frac{1}{2}\left(\frac{z-\mu}{\sigma}\right)^2}$$

Is the probability density function of a Gaussian distribution with mean μ and standard deviation σ, and the parameters α, μ_1, μ_2, σ_1, and σ_2 are functions of δ [4]. The SBM uses distinct functions for characteristic lengths greater than 11 cm (large particle distribution) and those below 8 cm (small particle distribution). In the interval from 8 cm to 11 cm, the SBM uses a bridging function to determine which parameter function to use [7]:

$$r_0 = 10(\delta + 1.05)$$

The SBM compares a uniform random number on [0, 1), r, to r_0, and if larger, uses the large particle distribution, otherwise it uses the small particle distribution.

After the particle distribution (small or large) has been chosen, χ is drawn by drawing a uniform random number on [0, 1) to select between the Gaussian distributions characterized by (μ_1, σ_1) and (μ_2, σ_2) for computing the area to mass ratio. Fig. 3 shows the resulting fragment area-to-mass distribution.

The SBM characterizes the fragment delta velocity $(m \cdot s^{-1})$ using a normal distribution for $\nu = 10\log_{10}\Delta v_F$ parametrized on χ:

$$pdf_\nu = \mathcal{N}(\nu; 0.2\chi + 1.85, 0.4)$$

This distribution is show in Fig. 4.

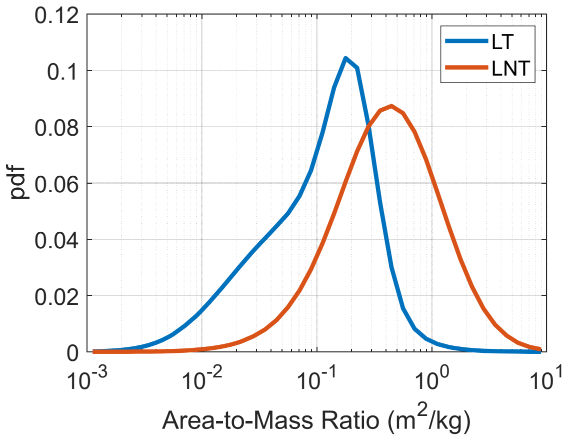

Fig. 3. Area-to-Mass Distribution

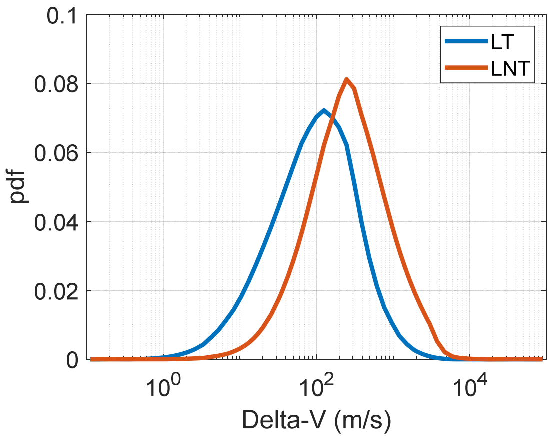

Fig. 4. *Delta-V Distribution*

The orbital elements for each fragment are obtained by uniformly distributing each delta-V vector over a sphere and adding it to the fragmenting object's state vector [8, 9]. It is assumed that fragments with perigee less than 100 km have reentered. Fig. 5 shows the distributions of fragment mean altitudes and inclinations, respectively, relative to those of the colliding satellites. For these figures, the fragmenting object is modeled in a 1,200 km, 45° inclination, circular orbit.

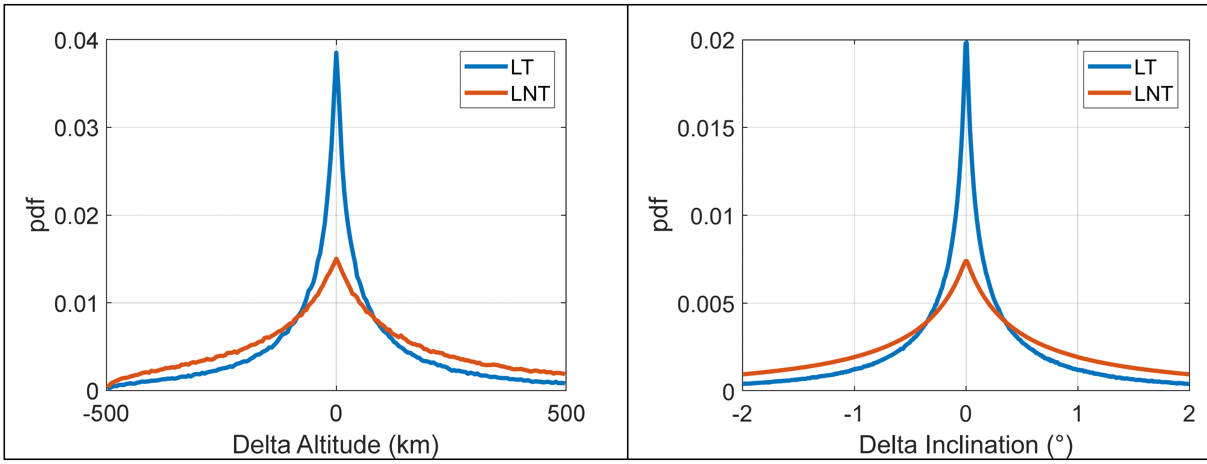

Fig. 5. Distributions of Fragment Mean Altitude and Inclination Relative to Those of Colliding Object

2.2 Decay Model

Following [10], the changes in semi-major axis (a), eccentricity (e), inclination (i), right ascension of ascending node (Ω), and argument of perigee (ω) over one revolution due to drag are:

$$\Delta a = -2\pi\delta a^2\rho\left(I_0 + 2eI_1 + \frac{3e^2}{4}(I_0 + I_2) + \frac{e^3}{4}(3I_1 + I_3)\right)exp(-c)$$

$$\Delta e = -2\pi\delta a\rho\left(I_1 + \frac{e}{2}(I_0 + I_2) - \frac{e^2}{8}(5I_1 - I_3) - \frac{e^3}{16}(5I_0 + 4I_2 - I_4)\right)exp(-c)$$

$$\Delta i = -\frac{\pi a\omega_\oplus\delta\rho}{2\eta\sqrt{Q}} sin\, i\,(I_0 - 2eI_1 + (I_2 - 2eI_1)\,cos(2\omega))\,exp(-c)$$

$$\Delta\mathit{\Omega} = -\frac{\pi a\omega_\oplus\delta\rho}{2\eta\sqrt{Q}}(I_2 - 2eI_1)\sin(2\omega)\exp(-c)$$

$$\Delta\omega = -\Delta\Omega\cos i$$

where:

$$c = \frac{ae}{H}$$

$$\delta = Q\frac{A}{m}C_D$$

$$Q = 1 - \frac{2\omega_\oplus(1-e)^{3/2}\cos i}{\eta\sqrt{1+e}}$$

Δa has units of km, Δe is unitless, and Δi, $\Delta\mathit{\Omega}$, and $\Delta\omega$ have units of rad
$\omega_\oplus$ is the Earth's rotation rate ($rad \cdot s^{-1}$)
H is the scale height at perigee (km)
η is the mean motion ($rad \cdot s^{-1}$)
C_D is the drag coefficient (2.2)
$\frac{A}{m}$ is the area-to-mass ratio ($m^2 \cdot kg^{-1}$)
ρ is the atmospheric density at perigee ($kg \cdot m^{-3}$)
I_s is the modified Bessel function of the first kind of order S evaluated at c.

The scale height (km) at perigee is:

$$H = \frac{R_{gas}T_{1/2}}{1000Mg}$$

where:

R_{gas} is the molar gas constant ($J \cdot K^{-1} \cdot mol^{-1}$)
M is the mean molecular weight at perigee ($kg \cdot mol^{-1}$)
g is the standard Earth gravity ($m \cdot s^{-2}$)

Jacchia 1977 model [11] is used to compute the atmospheric density and mean molecular weight at perigee.

The mean exospheric temperature is related to the $F10.7$ solar flux index by

$$T_{1/2} = 5.48\bar{F}^{0.8} + 101.8F^{0.4}$$

where:

$$\bar{F}(t_0) = \frac{\sum w(t)F(t)}{\sum w(t)}$$

$$w(t) = exp\left[-\left(\frac{t - t_0}{\tau}\right)^2\right]$$

τ is the averaging time (71 days)
F is the 10.7 cm solar flux index (sfu)

An eighth order Fourier series fit to daily historical data collected from 1 January 1947 to 13 November 2023 [12] is used to model the solar flux index, F, as shown in Fig. 6.

The atmospheric density as a function of altitude is computed using the following procedure:

1. Compute the temperature profile from the exospheric temperature.
2. Use an empirical mean molecular mass profile and initial atmospheric density at $z = 90$ km to compute the atmospheric density at $z = 100$ km by solving the barometric equation using the initial condition at $z = 90$ km.
3. Use the diffusion equations to solve for the number densities of species other than hydrogen at $z = 500$ km by solving the diffusion equation using the initial condition at $z = 100$ km.
4. Use the diffusion equations again to solve for the number densities of all species (including Hydrogen) at the desired altitude using the initial conditions at $z = 500$ km.
5. Compute the atmospheric density from the number densities of the species at the desired altitude.

This method is computationally prohibitive to compute at each simulation time step so instead, the atmospheric density as a function of altitude and exospheric temperature is precomputed on a uniform grid in (z, T_∞) and the simulation uses bilinear interpolation to obtain the value at the desired altitude given the current exospheric temperature. A heatmap of the atmospheric density data used in the bilinear interpolation is shown in Fig. 7.

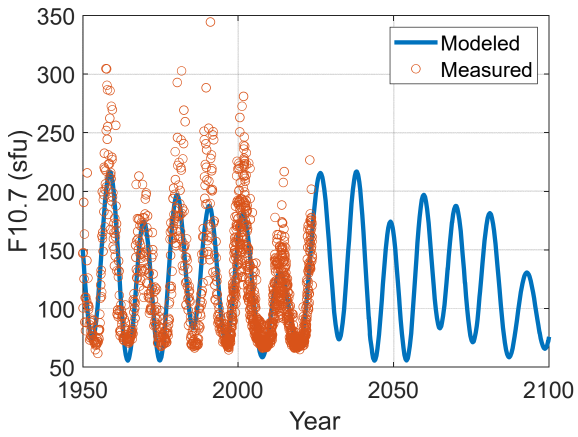

Fig. 6. Modeled F10.7 Solar Flux Index

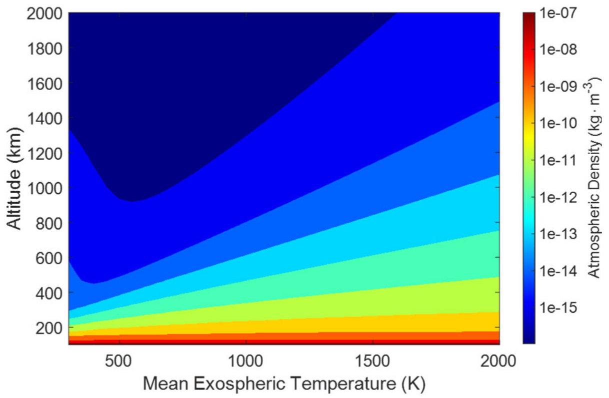

Fig. 7. Atmospheric Density as a Function of Mean Exospheric Temperature and Altitude

2.3 Gravity Model

To first order, the secular rate of change of right ascension of ascending node (Ω) and argument of perigee (ω) due to non-uniform Earth gravity are [13]:

$$\frac{\mathrm{d}\Omega}{dt} = -\frac{3}{2}J_2\frac{nR_E^2}{a^2(1-e)^2}\cos i$$

$$\frac{d\omega}{dt} = \frac{3}{4}J_2\frac{nR_E^2}{a^2(1-e)^2}(4-5sin^2 i)$$

where:

$$n = \sqrt{\frac{\mu}{a^3}}$$

J_2 is the second zonal coefficient (0.00108263)
R_E is the Earth's semi-major axis (km)
μ is the Earth's gravitational parameter ($km^3 \cdot s^{-2}$)

2.4 Encounter Rate Model

Following [14], the instantaneous average encounter rate between a satellite object A and a debris object B, is given by

$$r_E = \frac{n_A}{2\pi}\left(\frac{d_{HB}}{R_S}\right)^2 \int\limits_{\mathcal{H}} \frac{M(\nu_B, e_B)}{2\pi}\,\mathrm{d}\nu_B$$

where

n_A is the mean motion of orbit A ($rad \cdot s^{-1}$)
d_{HB} is the sum of the hard body radii of the two objects (km)
R_S is the screening radius (km)
e_B is the eccentricity of orbit B
ν_B is the B object's true anomaly (rad)
$M(\nu, e)$ is the mean anomaly (rad) calculated from true anomaly, ν (rad), and the eccentricity, e, as [13]

$$M(\nu, e) = \frac{(1-e^2)^{3/2}}{\left(1 + e\,cos(\nu)\right)^2}$$

$\mathcal{H}$ is the set of orbit B true anomalies such that the distance between the orbit B position and the closest point on orbit A is less than or equal to the screening radius.

Assuming the collisions follow a Poisson arrival process, the probability of at least one satellite encounter during an interval is given by

$$P_C = 1 - e^{-\tau N_S r_E}$$

where:

N_S is the number of satellites
τ is the interval duration (s)

3. SIMULATION

The simulation operates in two modes. In the "Fragmentation Impact" mode, the simulation determines the impact of initial fragmentation events in one constellation shell to a debris collision rate metric in all the constellation shells. This metric is defined as the collision rate between a satellite in a constellation shell and debris objects with sufficient specific energy to fragment the satellite. In the MC (Monte Carlo) mode, collision events leading to subsequent fragmentations are simulated based on the evolving collision rates. The simulation steps are:

1. Initialize background LEO debris objects from SATCAT
2. For each timestep
    a. Propagate debris objects over timestep using models in Sections 2.2 and 2.3
    b. For each constellation shell being simulated
        i. Determine background debris objects with sufficient specific energy to fragment satellites in current shell
        ii. Calculate the encounter rate and probability collision using the model in Section 2.4
3. For each trial
    a. Generate initial fragments using the model in Section 2.1
    b. For each timestep
        i. Propagate debris objects and non-maneuverable satellites (if any) using the models in Sections 2.2 and 2.3
        ii. For each constellation shell being simulated
            1. Determine background debris objects with sufficient specific energy to fragment satellites in current shell
            2. Calculate the encounter rate and probability collision using the model in Section 2.4
            3. If MC mode
                a. Draw uniform random variable to determine if a collision has occurred
                    i. Reduce the collision probability of a maneuverable satellite to account for collision avoidance reliability
                    ii. The collision probability of a non-maneuverable satellite is not reduced, as non-maneuverable satellites cannot avoid collisions
        iii. If MC mode
            1. Generate fragments for each collision using the model in Section 2.1

4. PARAMETERS

The initial parameters are summarized in Tab. 1. The start date is used to determine the solar flux at each time step, which is used to compute the atmospheric density used in Section 2.2. Two values are evaluated, January 2025 which is near a solar maximum (debris decay more quickly), and January 2030 which is near a solar minimum (debris decay more slowly), to bound the results.

A 3-year duration was selected to focus on near-term economic and tactical events. The time step and number of Monte Carlo trials were selected to provide reasonable simulation fidelity with fixed time step integration. The collision avoidance reliability of 99.99% includes the SST, SSA, and STM reliabilities.

Tab. 1. Initial Parameters

Parameter	Value
Start Date	$2025, 2030$
Duration	$3\ years$
Timestep	$5\ days$
Number of Trials	30
Screening Radius, R_S	$25\ km$
Drag Coefficient, c_d	2.2
Fragmentation Threshold	40 J/g
Collision Avoidance Reliability	99.99%

Five constellations are considered: Starlink 1st Generation (4,408 satellites), Starlink 2nd Generation (29,988 satellites), Kuiper (3,232 satellites), OneWeb 1st Generation (646 satellites), and Lightspeed (198 satellites). The altitude/inclination pairs (shells) for each constellation, and associated span, mass, and average cross-sectional area parameters, are shown in Tab. 2. The modeled physical characteristics of the Starlink and OneWeb satellites are based on satellites currently in orbit [15]. The Starlink 2nd generation satellites described are the "Mini" version currently being launched on Falcon 9 rockets. SpaceX filings indicate the "Starship" version of the 2nd generation satellites would have substantially greater mass (2,000 kg) and average cross-sectional area (147 m^2) [16]. It is expected that the results for Starlink would be meaningfully worse if satellites with those characteristics are deployed.

The Kuiper parameters are based on the values for the demonstration satellites launched in 2023 [15], the production satellites expected to be deployed may be meaningfully larger, which would affect the simulation results. The Lightspeed parameters are extrapolated from the published 750 kg mass [17]. Not modeled in this paper, the "steady state" of each constellation includes both "rising" satellites during orbit raising, and "setting satellites" in the process of de-orbit, and possibly "spare" satellites in orbit. For simplicity, and conservatively, those additional satellites are not considered in this analysis.

Tab. 2. Constellation Parameters

Constellation	**#Sats**	**Alt (km)**	**Inc (°)**	**Span (m)**	**Mass (kg)**	**Area (m^2)**
Starlink Gen 1 (SL1)	1584	540	53.3	8.86	260	13.56
	1584	550	53			
	520	560	97.6			
	720	570	70			
Starlink Gen 2 (SL2)	5280	340	55	29	750	33.88
	5280	345	46			
	5280	350	38			
	3600	360	96.9			
	3360	525	53			
	3360	530	43			
	3360	535	33			
	144	604	148			
	324	614	115.7			
Kuiper (K)	782	590	33	10	600	10.3
	1292	610	42			
	1156	630	51.9			
OneWeb (OW)	648	1200	87.9	5	148	2.96
Lightspeed (LS)	198	1325	50.9	8.5	750	6.6

5. RESULTS

The background collision rate and probability of collision are determined in Section 5.1. Section 5.2 uses these *background levels* to determine the sensitivity of each constellation shell to *initial fragmentation* events in any shell. In section 5.3, Monte Carlo simulations are used to explore the impact of *subsequent collisions* when satellites in constellation shells are rendered *non-maneuverable* for any reason.

5.1 Background Collision Rate and Probability of Collision During a Month

Fig. 8 is a heatmap of the background collision rate for an *individual* satellite in each of the constellation shells. Background objects are debris in the satellite catalog [18]. Collisions are defined as a debris object impacting a satellite with sufficient specific energy to catastrophically fragment it. Similar to a debris flux metric, potential avoidance by active satellites is not considered. The shells are denoted on the left side of each plot by SL1 for 1st Generation Starlink constellation shells, SL2 for 2nd Generation Starlink constellation shells, K for Kuiper constellation shells, OW for 1st Generation OneWeb constellation shells, and LS for Lightspeed constellation shells. The constellation designation is followed by the shell's nominal altitude and inclination.

The plot on the left side of Fig. 8 is for a start date of January 2025, near a solar maximum, and the plot on the right side is for a January 2030 start date, near a solar minimum. For both plots, the collision rates for shells above 600 km show little, or no, change over the 3-year timeframe as the effects of drag are negligible. Lower shells on the right side generally show a decreasing collision rate over time as drag reduces the number of debris objects that satellites interact with, while those on the left side show less variation over the 3-year timeframe, as the effects of drag are reduced near a solar minimum. There is also an increase in collision rate in the lower shells as the debris above decay, which is more pronounced on the right side with higher drag near a solar minimum.

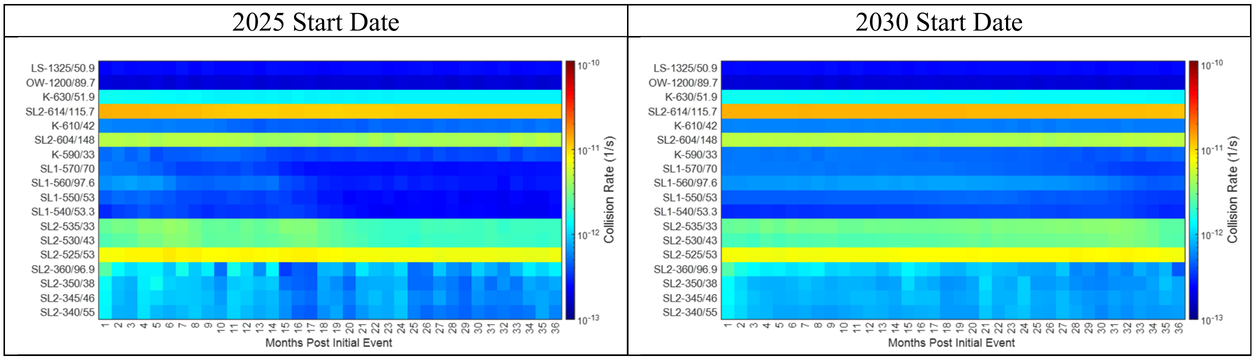
2025 Start Date

2030 Start Date

Fig. 8. Background Collision Rate

Fig. 9 shows the probability of a collision occurring with a background debris object in each *month*, taking into account the *number of satellites in each shell* and the number of seconds in a month. The left-side and right-side plots show similar variations to those in Fig. 8 due to the differences in drag. While the highest background collision rate in in the SL2-614/115.7 shell, the highest probability of collision during a month is in the SL2-525/53 shell. This is due to the significantly greater number of satellites in that shell, 3,360 versus 324.

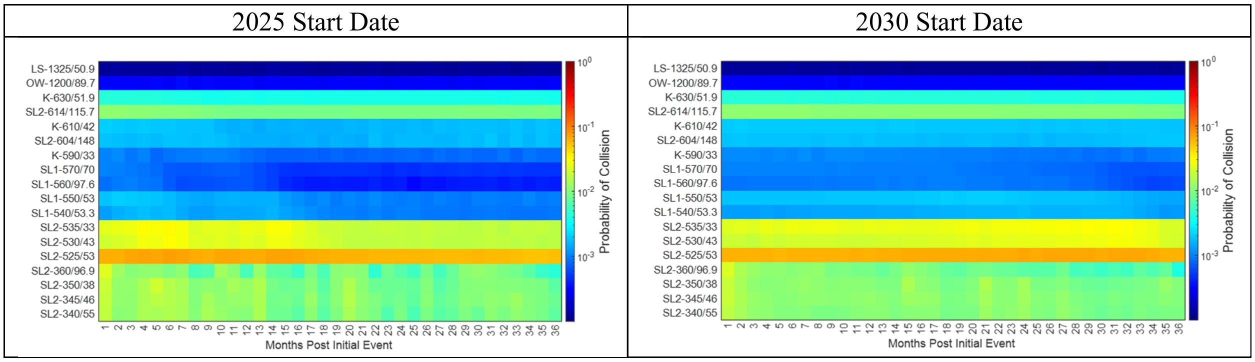
2025 Start Date

2030 Start Date

Fig. 9. Background Probability of Collision During Month

5.2 Fragmentation Impact on Collision Rate

The impact of fragmentation events on collision rate is explored by fragmenting one, three, and ten satellites in a constellation shell, and observing the increase in collision rate relative to the background rates in each of the constellation shells. Results are shown for fragmentation events in five of the constellation shells, selected as illustrative examples, in Fig. 10, Fig. 11, Fig. 12, Fig. 13, and Fig. 14. The plots on the left side of each figure are for a Tab. 3 provides a summary for each of the cases.

Tab. 3. Fragmentation Impact Summary

	Shell	#Events	Approximate Collision Rate Impact
Fig. 10	SL1-550/53	1	• 2X in the surrounding orbits
		3	• 3X in SL1-550/53, adjacent SL1-540/53.3, and similar inclination SL2-525/53 • 25% to 50% in other two SL1 shells
		10	• 10X in three shells with similar inclination • 20% in other shells, except OW and LS
Fig. 11	SL2-530/43	1	• 5X in SL2-530/43 for a few months • 2X in adjacent SL2 shells for a few months
		3	• 15X in SL2-530/43 decreasing to 7X in 3 years • Less significant impact to other shells between 525 and 550 km
		10	• 50X in SL2-530/43 decreasing to 20X in 3 years • Significant impacts in other shells between 525 and 550 km • Up to 8X impact in VLEO shells as debris decay through them
Fig. 12	SL2-350/38	1	• 17X initial impact to SL2-350/38, impact lasts a few months to over a year depending on the solar cycle • Reduced impact to other VLEO shells
		3	• 36X initial impact to SL2-350/38, impact lasts a few months to over a year depending on the solar cycle • Reduced impact to other VLEO shells
		10	• 100X initial impact to SL2-350/38, impact lasts a few months to a few years depending on the solar cycle • Reduced impact to other VLEO shells
Fig. 13	K-610/42	1	• 3X in K610/42 • 40% in 2 adjacent shells on each side
		3	• 7X in K610/42 • Impact to shells between 525 and 630 km
		10	• 20X in K610/42 • Increased impact to shells between 525 and 630 km
Fig. 14	LS-1325/50.9	1	• 8X in LS shell • Slight impact in OW shell
		3	• 18X in LS shell • Slight impact in OW shell
		10	• 55X in LS shell • 40% impact in OW shell

Fragmentations in a shell significantly increase the collision rates in that shell, by a factor of 2 to 17 for one fragmentation, by a factor of 3 to 36 for three fragmentations, and by a factor of 10 to 100 for ten fragmentations. These increases persist for months to a year in shells below 400 km, for centuries in the LS and OW shells, and for years to decades in the other shells. Increased collision rates proportionally increase collision risk for both maneuverable satellites (which can avoid collisions) and non-maneuverable satellites (which cannot avoid collisions).

Fragmentations not only impact the shell they occur in, but also shells with similar altitude or inclination. Fragmentations in the SL1-550/53 shell have peak impact to collision rates in the SL2-525/53 shell. The impacts in the SL1-550/53 and SL1-540/53.3 shells, while still significant, are slightly less.

Fragmentations in VLEO shells (the four SL2 shells between 340 and 360 km) do not significantly impact the higher shells. The fragments decay within months to a year depending on the solar cycle. Fragmentations in the OW and LS shells do not significantly impact the lower shells during the three-year timeframe considered. Fragments in these shells typically take centuries to decay. Fragmentations in the shells between 525 and 630 km do not significantly impact the OW and LS shells but do increase collision rates in the VLEO shells as the fragments decay through them over months to years depending on the fragmentation altitude and solar cycle.

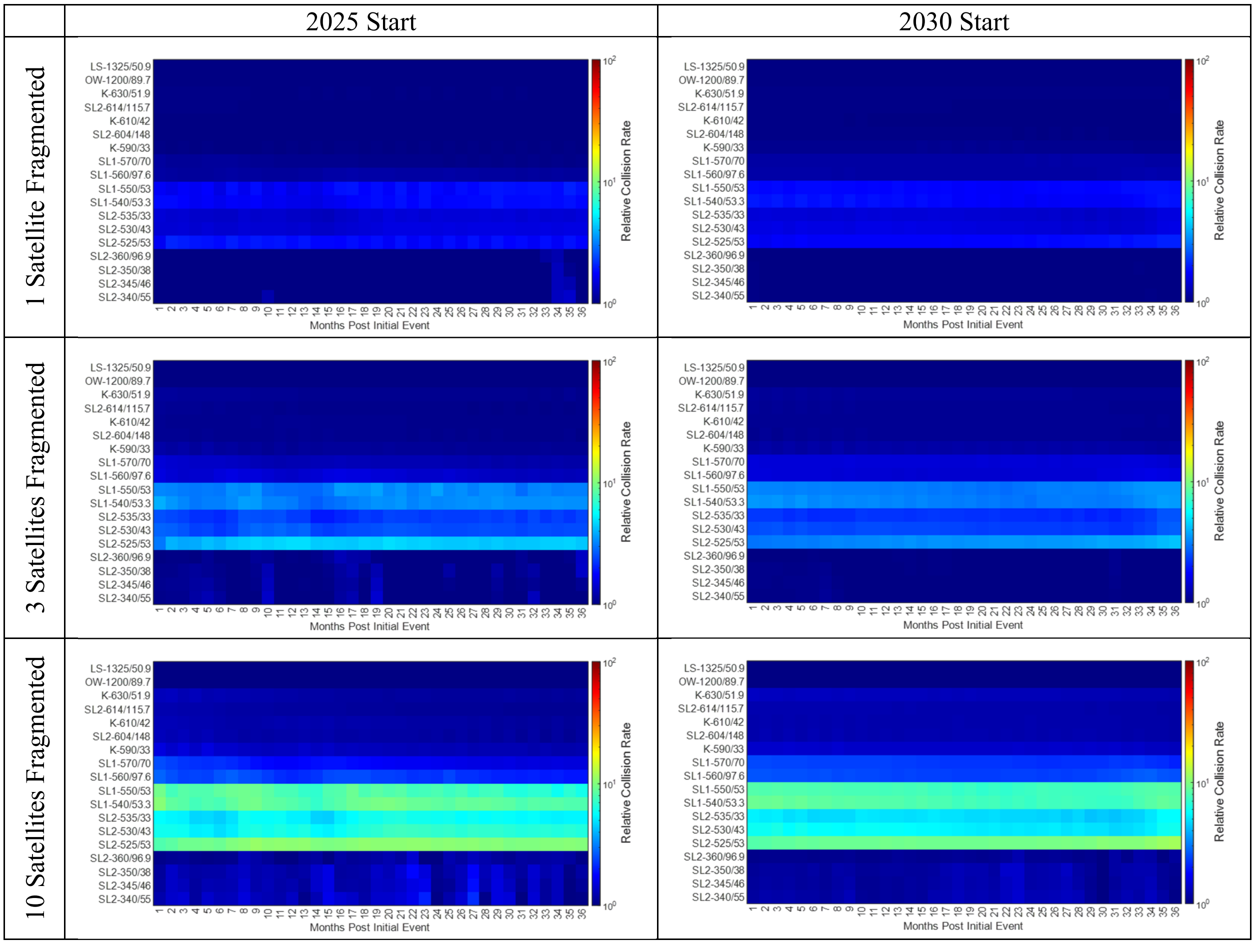

Fig. 10. Relative Collision Rate Following Fragmentation of Satellites in SL1-550/53 Shell

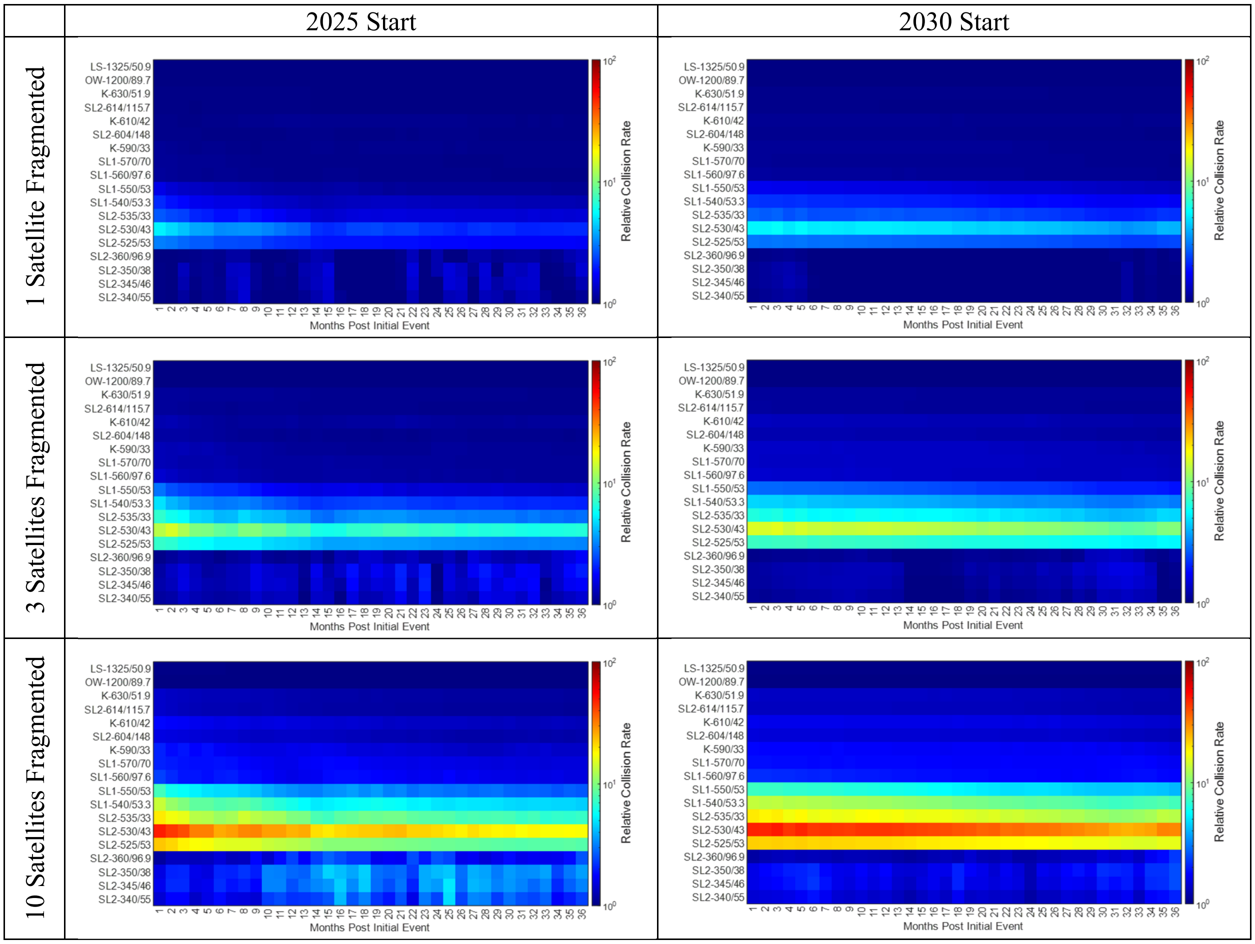

Fig. 11. Relative Collision Rate Following Fragmentation of Satellites in SL2-530/43,

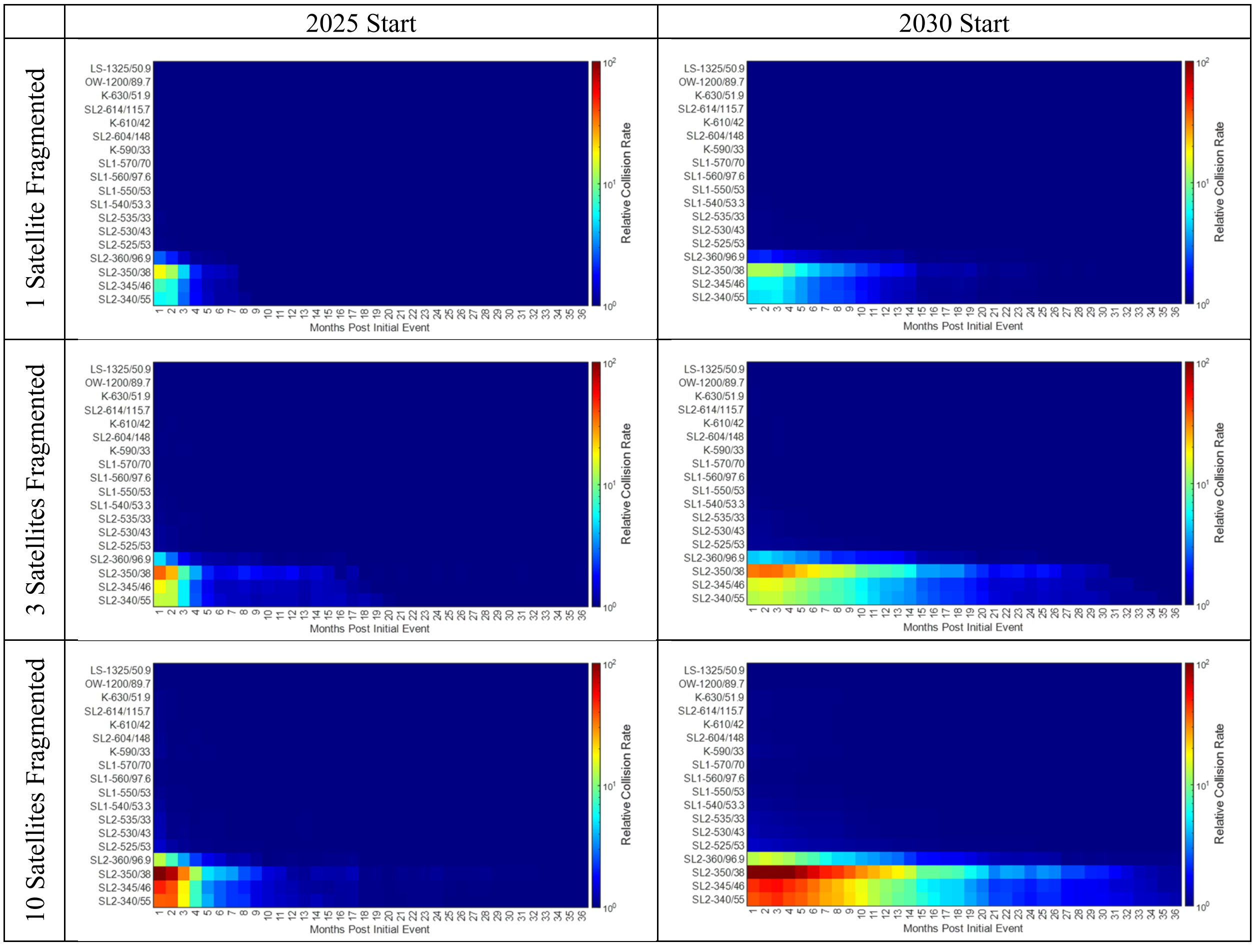

Fig. 12. Relative Collision Rate Following Fragmentation of Satellites in SL2-350/38

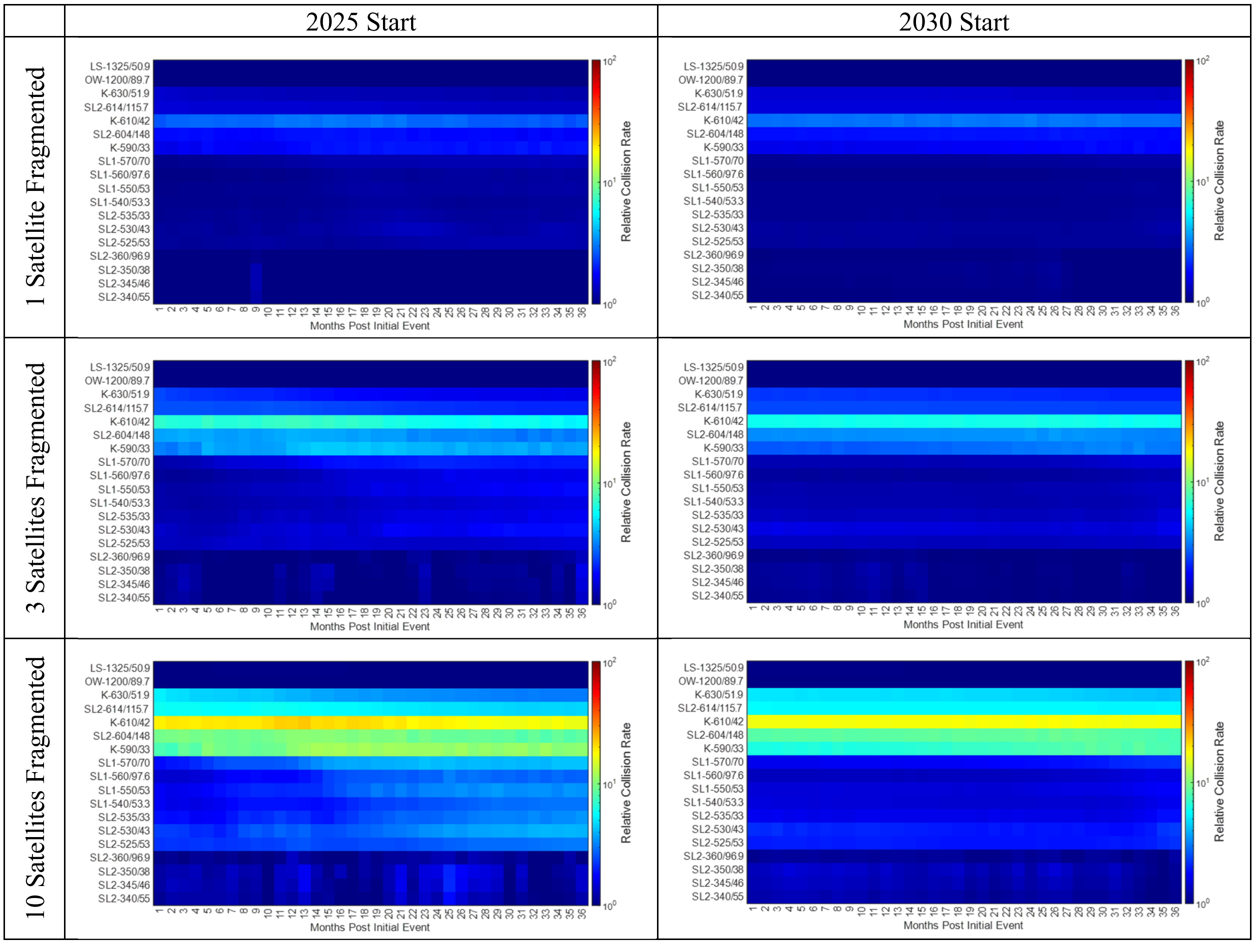

Fig. 13. Relative Collision Rate Following Fragmentation of Satellites in K-610/42

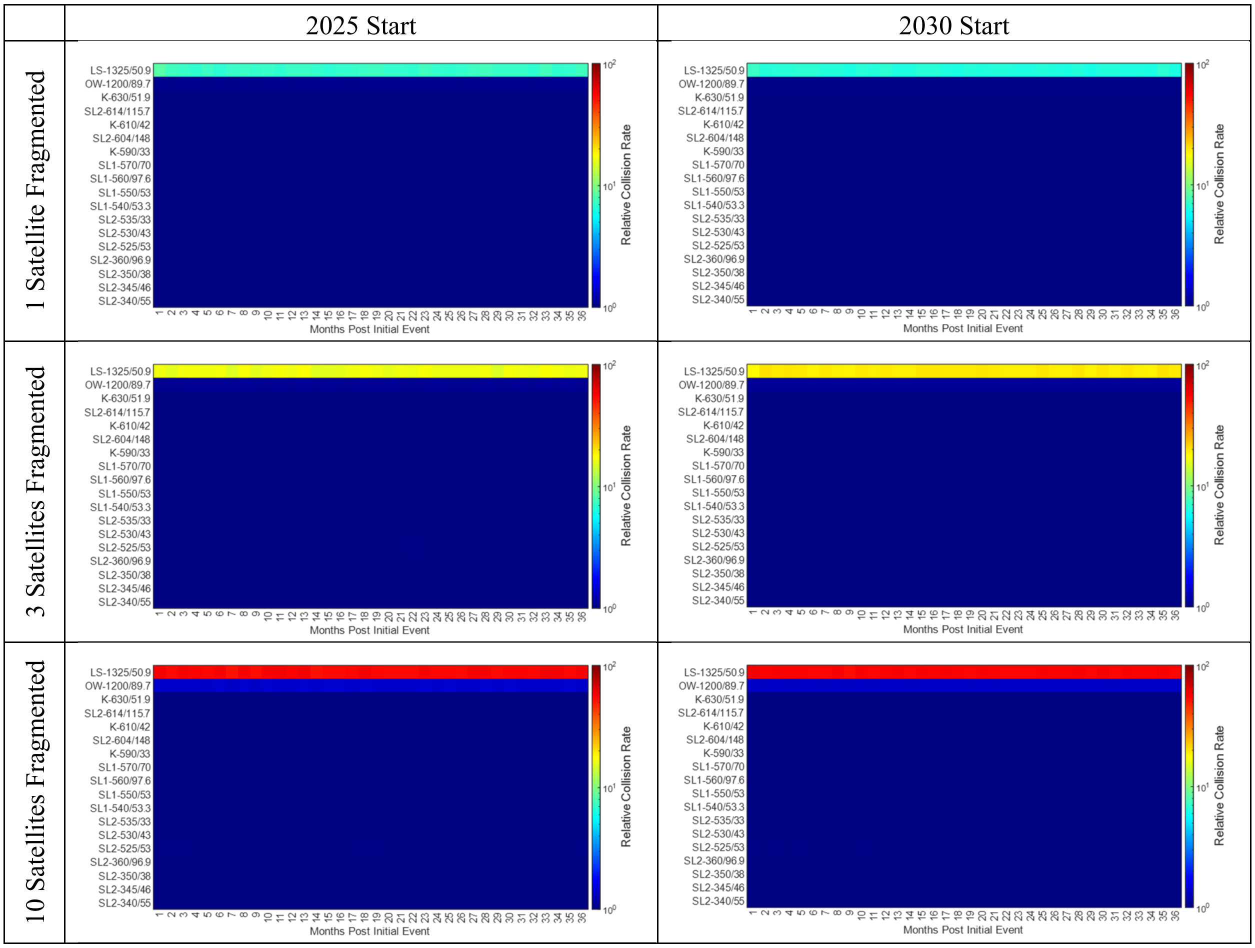

Fig. 14. Relative Collision Rate Following Fragmentation of Satellites in LS-1325/50.9

5.3 Impact of Subsequent Collisions

The impact of initial fragmentations in combination with rendering satellites in a constellation non-maneuverable is explored using a Monte Carlo simulation. Satellites may be rendered non-maneuverable due to a range of intentional or unintentional attacks or factors, such as very high levels of radiation, cyber-attacks, or latent defects.

In the first example, three satellites in the SL1-550/53 shell are fragmented in January 2030 and simultaneously, the satellites in the SL2 constellation are rendered non-maneuverable. The results are shown in Fig. 15 and Fig. 16. Fig. 15 is a collision map, showing the average number of collisions that occurred involving satellites from each constellation shell *during each month*. It shows numerous collisions occurring with satellites from the SL2-535/33, SL2-530/43, and SL2-525/53 shells. This is especially the case in the SL2-525/53 shell, which has the same inclination as the initially fragmented satellites. Fig. 16 shows the cumulative number of collisions over time, with vertical bars for 5%, 50%, and 95% of the trials. It shows that 95% of the trails resulted in over 250 collisions and 5% exceeded 325 collisions within 3 years.

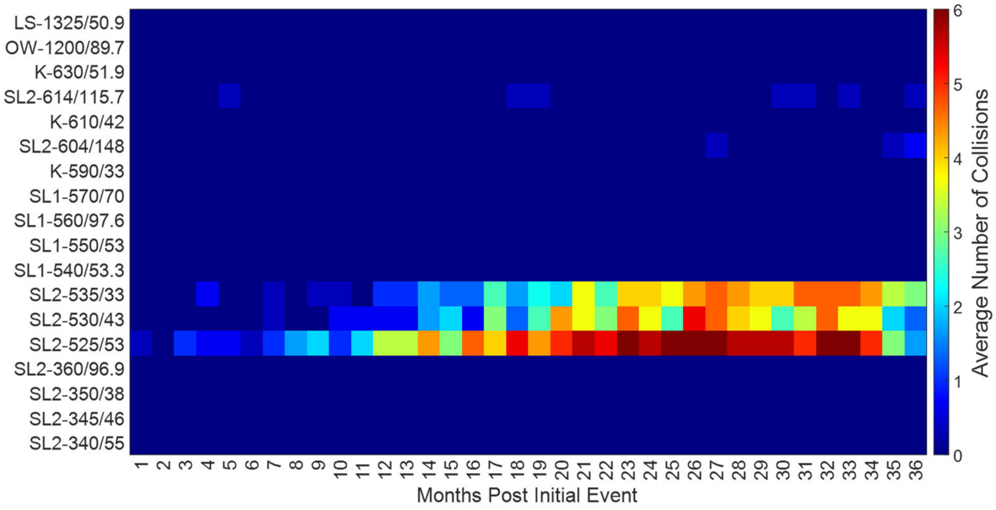

Fig. 15. Collision Map Following Fragmentation of Three Satellites in SL1-550/53 With SL2 Satellites Rendered Non-Maneuverable (January 2030 Initial Fragmentation)

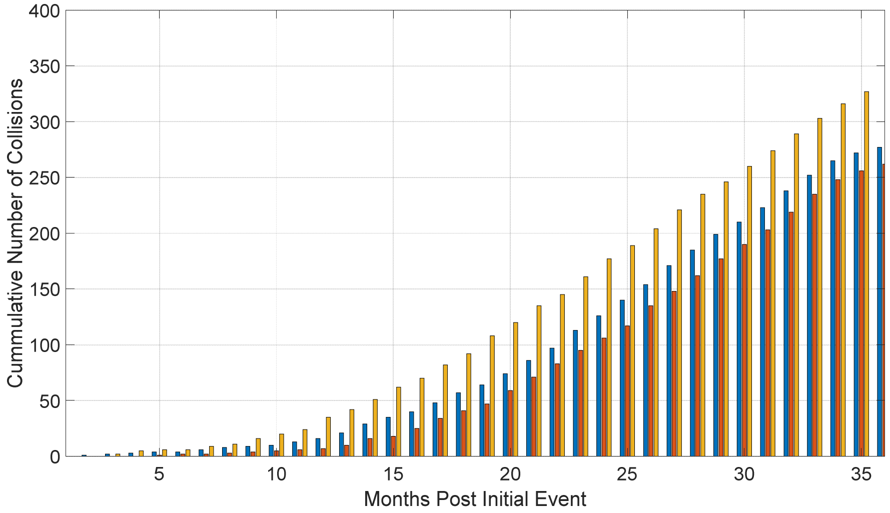

Fig. 16. Cumulative Collisions Following Fragmentation of Three Satellites in SL1-550/53 With SL2 Satellites Rendered Non-Maneuverable (January 2030 Initial Fragmentation)

In the second example, three satellites in the SL1-530/43 shell are fragmented in January 2030 and simultaneously, the satellites in the SL2 constellation are rendered non-maneuverable. The collision map, Fig. 17, shows numerous collisions occurring with satellites from the SL2-535/33, SL2-530/43, and SL2-525/53 shells. Fig. 18 shows that 95% of the trails resulted in over 295 collisions and 5% exceeded 397 collisions within 3 years.

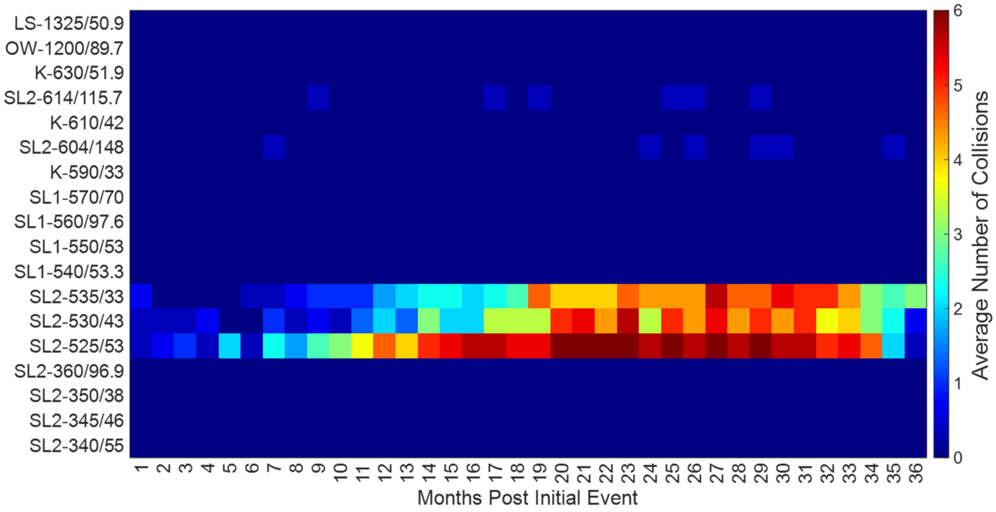

Fig. 17. Collision Map Following Fragmentation of Three Satellites in SL2-530/43 With SL2 Satellites Rendered Non-Maneuverable (January 2030 Initial Fragmentation)

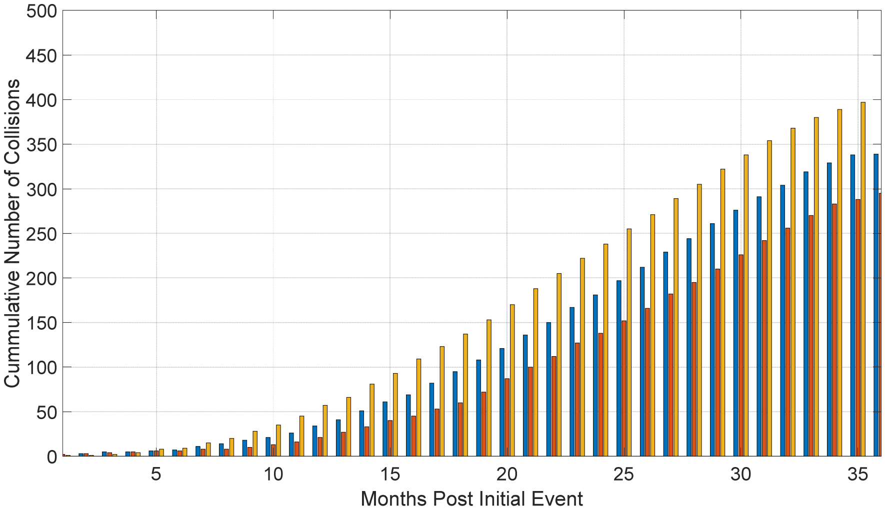

Fig. 18. Cumulative Collisions Following Fragmentation of Three Satellites in SL2-530/43 With SL2 Satellites Rendered Non-Maneuverable (January 2030 Initial Fragmentation)

In the two examples, it is seen that interactions between fragmentation events and loss of maneuverability can result in hundreds of catastrophic collisions over the three-year period evaluated in this paper.

6. CONCLUSIONS

A model was developed for examining the extent to which fragmentation events in one LEO constellation shell impact collision rates in that shell and other LEO shells, and for examining the impact of satellites in specific constellation shells being rendered non-maneuverable (regardless of the cause) in conjunction with related or unrelated fragmentation events. The results generated are based on the models described, associated assumptions, and inputs; and any quantitative conclusions drawn are intended to be interpreted as such.

Fragmentations in a large LEO constellation shell are observed to:

- Significantly increase the collision rates in that shell, by as much as two orders of magnitude for ten fragmentations
- Result in increased collision rates that can persist for a year to centuries depending on altitude of the fragmentation shell.
- Increase collision rates for both maneuverable satellites and non-maneuverable satellites.
- Not only adversely impact the shell they occur in, but also impact shells with similar altitude or inclination.
- Produce not just trackable debris, but also produce an order of magnitude more lethal, non-trackable (LNT) debris.

This is true regardless of whether the fragmentations result from accidents (collisions, explosions), intentional attacks (kinetic, directed energy, cyber), latent design or production defects, or even as a consequence of natural phenomena (meteorites, solar events). Interactions between fragmentation events and loss of maneuverability (regardless of the cause) can result in hundreds of catastrophic collisions over the three-year period evaluated in this paper.

Fragmentations in the shells between 525 and 630 km increase collision rates in the 340, 345, 350, and 360 km shells as the fragments decay through them over months to years depending on the fragmentation altitude and solar cycle, but do not significantly impact the 1,200 and 1,325 km shells. Fragmentations in the 340, 345, 350, and 360 km shells do not significantly impact the higher shells, and fragmentations in the 1,200 and 1,325 km shells do not significantly impact the lower shells. This suggests the possibility of improving resilience by employing one shell in each of very low LEO, low LEO, and high LEO regions, rather than multiple shells in a single orbital region.

These results suggest that additional work is needed to consider situations that could be meaningfully more serious, such as evaluating the effects of fragmentation events:

- Taking into account future versions of certain mega-constellations (e.g. Starship version of 2nd Generation satellites, and Kuiper production satellites).
- On the safety of the ISS and other manned platforms.
- Resulting from highly targeted kinetic attacks as a special form of fragmentation event intended to maximize consequential damage.
- On carrying capacity over longer time horizons, identifying “tipping points” that may render certain orbital neighborhoods effectively unusable for decades or centuries, and accounting for additional constellations that are planned and/or in development that will also occupy orbital neighborhoods near those considered here.
- Evaluate the effects of fragmentation events to carrying capacity over longer time horizons.
- On the short-, mid- and long-term mission functional efficacy of constellations in the face of fragmentation events (i.e. functional resiliency).

Probably the single most important result from this work is data illustrating that *more is not necessarily better* when it comes to highly proliferated LEO constellations. It is anticipated that there may be very important implications for constellation design, orbital allocations, national security, and other policies that have not necessarily been well considered in the presence of very large mega-constellations.

7. REFERENCES

[1] Daniel L. Oltrogge, Salvatore Alfano, and Robert Hall, Comparison of predicted and observed spacecraft encounters from Russian ASAT test, *2022 Advanced Maui Optical and Space Surveillance Technologies Conference (AMOS*), September 2022.
[2] M. A. Sturza, M. D. Dankberg, & W. N. Blount, LEO Capacity Modeling for Sustainable Design, *2022 Advanced Maui Optical and Space Surveillance Technologies Conference (AMOS*), September 2022.

[3] D. Jang, A. D'Ambrosio, M. Lifson, C. Pasiecznik, & R. Linares, Stability of the LEO Environment as a Dynamical System, *2022 Advanced Maui Optical and Space Surveillance Technologies Conference (AMOS)*, September 2022.

[4] N. L. Johnson, P. Krisko, J.-C. Liou, & P. Anz-Meador. NASA's new breakup model of evolve 4.0. *Advances in Space Research*. 28. 1377-1384, 2001.

[5] P. Krisko, Proper Implementation of the 1998 NASA Breakup Model. *NASA Orbital Debris Quarterly News*, Volume 15, Issue 4., 2011.

[6] T. Maclay, & D. McKnight, Space environment management: Framing the objective and setting priorities for controlling orbital debris risk. *Journal of Space Safety Engineering*, 8(1), 93-97, 2021.

[7] A. Horstmann, S. Hesselbach, C. Wiedemann, S. Flegel, & M. Oswald. Final Report – Enhancement of S/C Fragmentation and Environment Evolution Models. DD-0045, *Institute of Space Systems*, Technische Universität Braunschweig, 2020.

[8] R. Klima, D. Bloembergen, R. Savani, K. Tuyls, A. Wittig, A. Sapera, & L. Summerer, Game Theoretic Analysis of the Space Debris Removal Dilemma (*CCN*), 2018.

[9] S. Frey & C. Colombo Transformation of satellite breakup distribution for probabilistic orbital collision hazard analysis. *Journal of Guidance, Control, and Dynamics*, 44(1), 88-105, 2021.

[10] L. Blitzer, *Handbook of Orbital Perturbations*. Tucson, AZ: University of Arizona, 1970.

[11] L. G. Jacchia, Thermospheric Temperature, Density and Composition: New Models. Smithsonian Astrophysical Observatory, Special Report 375, 1977.

[12] LASP Interactive Solar Irradiance Datacenter, Penticton Solar Radio Flux at 10.7 cm. *National Research Council Canada (NRC)*, 2023. https://lasp.colorado.edu/lisird/data/penticton_radio_flux

[13] A. Vallado, *Fundamentals of Astrodynamics and Applications*, Fourth Edition, Microcosm Press, 2013.

[14] S. Alfano, D. Oltrogge, Volumetric assessment of satellite encounter rates, *Acta Astronautica*, Volume 152, Pages 891-907, 2018.

[15] ESA. DISCOSweb Objects, 2024. https://discosweb.esoc.esa.int/objects

[16] D. Goldman, Letter to Merlene H. Dortch, Re: IBFS File Nos. SAT-LOA-20200526-00055 and SAT-AMD-20210818-00105, October 2022.

[17] J. Rainbow, Telesat's initial LEO constellation fully funded after manufacturer switch. SpaceNews, 11 August 2023.

[18] Space-Track.org, Satellite Catalog. https://www.space-track.org/#catalog